Nano Research
2023, 16(4): 5973–5982

ISSN 1998-0124 CN 11-5974/O4
https://doi.org/10.1007/s12274-022-5298-y

Research Article

Stabilization of high-voltage layered oxide cathode by utilizing residual lithium to form NASICON-type nanoscale functional coating

Yabin Shen[1,2], Yingqiang Wu[5], Dongyu Zhang[1,2], Yao Liang[1,2], Dongming Yin[1,2], Limin Wang[1,2], Licheng Wang[3] (✉), Jingchao Cao[4] (✉), and Yong Cheng[1] (✉)

[1] *State Key Laboratory of Rare Earth Resource Utilization, Changchun Institute of Applied Chemistry, Chinese Academy of Sciences, Changchun 130022, China*
[2] *School of Applied Chemistry and Engineering, University of Science and Technology of China (USTC), Hefei 230026, China*
[3] *College of Physics Science and Technology, Yangzhou University, Yangzhou 225002, China*
[4] *Changsha Research Institute of Mining and Metallurgy Co., Ltd, Changsha 410012, China*
[5] *Institute of Nuclear and New Energy Technology, Tsinghua University, Beijing 100084, China*

Received: 20 September 2022 / **Revised:** 27 October 2022 / **Accepted:** 5 November 2022

ABSTRACT

High-voltage medium-nickel low-cobalt lithium layered oxide cathode materials are becoming a popular development route for high-energy lithium-ion batteries due to their relatively high capacity, low cost, and improved safety. Unfortunately, capacity fading derived from surface lithium residue, electrode-electrolyte interfacial side reactions, and bulk structure degradation severely limits large-scale commercial utilization. In this work, an ultrathin and uniform NASICON-type $Li_3V_2(PO_4)_3$ (LVP) nanoscale functional coating is formed in situ by utilizing residual lithium to enhance the lithium storage performance of $LiNi_{0.6}Co_{0.05}Mn_{0.35}O_2$ (NCM) cathode. The GITT and *ex-situ* EIS and XPS demonstrate exceptional Li^+ diffusion and conductivity and attenuated interfacial side reactions, improving the electrode-electrolyte interface stability. The variable temperature *in-situ* XRD demonstrates delayed phase transition temperature to improve thermal stability. The battery *in-situ* XRD displays the single-phase H1-H2 reaction and weakened harmful H3 phase transition, minimizing the bulk mechanical degradation. These improvements are attributed to the removal of surface residual lithium and the formation of NASICON-type $Li_3V_2(PO_4)_3$ functional coatings with stable structure and high ionic and electronic conductivity. Consequently, the obtained NCM@LVP delivers a higher capacity retention rate (97.1% vs. 79.6%) after 150 cycles and a superior rate capacity (87 mAh·g^{-1} vs. 58 mAh·g^{-1}) at a 5 C current density than the pristine NCM under a high cut-off voltage of 4.5 V. This work suggests a clever way to utilize residual lithium to form functional coatings in situ to improve the lithium storage performance of high-voltage medium-nickel low-cobalt cathode materials.

KEYWORDS

lithium-ion battery, high-voltage medium-nickel low-cobalt cathode, surface modification, residual lithium, NASICON-type $Li_3V_2(PO_4)_3$

1 Introduction

In the past few years, the high-nickel lithium layered oxides cathodes ($LiNi_xCo_yMn_{1-x-y}O_2$, NCM, x>0.6) have been regarded as the most prospective cathode material candidates for the development of high-energy-density Li-ion batteries owing to their relatively high output specific capacity [1, 2]. For example, $LiNi_{0.8}Co_{0.1}Mn_{0.1}O_2$ (NCM811) cathode material has been widely used in batteries for new energy vehicles [3, 4]. Whereas, high-nickel cathodes have severe safety and high cost issues due to high Ni content and relatively strict manufacturing process, which makes people worry about their use despite their high capacity [5, 6]. Recently, a large number of new energy vehicle fires and explosions have been reported around the world. Then a new development route for high-voltage medium-nickel low-cobalt cathode materials is proposed, which has the triple advantages of high capacity, high safety, and low cost, and is a promising alternative to high-nickel cathode materials [7, 8]. Nonetheless, it suffers from the same problem of rapid capacity fading due to unstable surface properties and inherent structure [9, 10]. For example, the residual lithium originated from the excess lithium added during lithiation calcination easily reacts with CO_2 and H_2O in the air during material storage, generating poisonous LiOH and Li_2CO_3 on the surface of the particle, which not only hinders the migration of lithium ions owing to the insulating property but also increases the viscosity of the slurry during the electrode preparation [11, 12]. Furthermore, the oxidative decomposition of Li_2CO_3 causes the evolution of CO_2 and CO gases upon cell charging, leading to safety concerns, while the reaction of LiOH with an electrolyte salt ($LiPF_6$) produces HF that leaches out transition metals [13]. In addition, high voltage means deep redox

Address correspondence to Licheng Wang, mx120200330@yzu.edu.cn; Jingchao Cao, changbaicao@126.com; Yong Cheng, cyong@ciac.ac.cn

reaction and deintercalation of lithium, which also brings greater challenges to the interface stability and bulk structure stability of the material [14, 15]. The deep redox reaction will produce more highly reactive and unstable Ni^{4+}, which tends to spontaneously obtain electrons from the lattice oxygen and be reduced to stable Ni^{2+}, especially on the surface of the material [16]. This not only promotes the loss of lattice oxygen atoms into highly active oxygen molecules, which in turn catalyzes the decomposition of the electrolyte but also causes harmful interfacial phase transitions (layered → spinel → rock salt phase), thereby increasing interfacial charge transfer resistance and reducing lithium diffusion kinetics [17, 18]. And the deep deintercalation of lithium increases the degree of expansion and contraction of the layered structure (i.e., the enhanced harmful H2 to H3 phase transition), which will bring about large anisotropic internal stress and cause the secondary aggregate particles to produce intergranular microcrack [19–21]. Then the increased contact area of the electrode electrolyte will further aggravate the side reaction of the interface, which will cause a sharp decline in the output capacity of the battery [22]. Therefore, finding a suitable modification strategy to improve the above problems is an important research direction to promote the practical application of high-voltage medium-nickel low-cobalt cathode materials.

Structural design [23, 24], bulk doping [25, 26], and surface coating [27, 28] are the most commonly used material modification strategies. In contrast, the surface coating modification can play a dual role in physically blocking the electrode electrolyte interface contact and constraining the expansion and contraction of the bulk structure, which can greatly improve the severe problems caused by the residual lithium and high voltage [29, 30]. Commonly used coating materials include metal oxide (Co_3O_4 [31], ZrO_2 [32]), metal fluoride (AlF_3 [33]), metal phosphate ($AlPO_4$ [34], BPO_4 [35]), lithium-ion conductor (Li_2ZrO_3 [36], $LiNbO_3$ [37]), organic conductive polymer (TNPP [38]), carbon (Graphene [39]), etc. They play the role of removing residual alkali, physically blocking electrode-electrolyte contact, preventing HF acid corrosion and active metal ions dissolution, enhancing interface lithium conductivity, and alleviating particle volume changes, respectively [40]. However, studies related to the elimination of residual lithium and the in-situ formation of functional coatings for NASICON-type fast ion conductor solid electrolytes have been rarely reported. Particularly, the NASICON-structured $Li_3V_2(PO_4)_3$ (LVP), as a superior solid electrolyte, presents ultrahigh Li^+ conductivity, benefitting from its unique phosphate structure with large interstitial spaces in an open framework and high stability with small volume variation [41–43]. Then the electrode-electrolyte interface environment and the bulk layered structure stability will be greatly improved, thereby enhancing the long-cycle stability and rate performance of the high-voltage medium-nickel low-cobalt cathode material.

In this work, we have successfully prepared a 1 wt.% ultrathin and uniform NASICON-structured $Li_3V_2(PO_4)_3$-coated high-voltage medium-nickel low-cobalt cathode $LiNi_{0.6}Co_{0.05}Mn_{0.35}O_2$ (NCM@LVP) through a two-step synthesis method of liquid phase stirring mixing and solid phase dry annealing. The NCM@LVP sample exhibits superior electrochemical properties in the 4.5 V high-voltage lithium-ion half/full batteries. And the excellent improvement effect is also fully elucidated by systematically comparing the properties of lithium diffusion kinetics, electrode-electrolyte interface stability, thermal stability, and layered structure stability of the pristine NCM and NCM@LVP material. Various characterization methods such as the GITT curves, CV curves of different scan rates, *ex-situ* EIS/XPS/SEM, the high temperature self-discharge test, the variable temperature *in-situ* XRD, and the battery *in-situ* XRD are used for exploration. We strongly recommend this surface modification method to effectively eliminate and utilize residual lithium to form functional coatings of NASICON structure-type materials. And the obtained NCM@LVP material will achieve the goals of high capacity, long life, high safety, and low cost.

2 Experimental

2.1 Materials preparation

The $LiNi_{0.6}Co_{0.05}Mn_{0.35}O_2$ sample was synthesized as we reported previously [44]. To obtain NCM@LVP material, first, 2 g of $LiNi_{0.6}Co_{0.05}Mn_{0.35}O_2$ sample was added to 15 mL of an aqueous solution containing 16.9 mg of dissolved $NH_4H_2PO_4$. Next, 15 mL of a mixed solution containing 11.5 mg H_4NO_3V and 24.7 mg $C_2H_2O_4{\cdot}2H_2O$ was added to the above solution. Then, the mixed solution was stirred and evaporated to dryness in a water bath at 80 °C. Finally, the obtained dry powder was annealed at 800 °C in the air (Fig. S1 in the Electronic Supplementary Material (ESM)). The calculated coating amount of $Li_3V_2(PO_4)_3$ is 1 wt.%.

2.2 Materials characterization

The particle morphology and element distribution were determined by scanning electron microscopy (SEM, Hitachi S-4800) and energy-dispersive X-ray spectrometer (EDS, Quantax 200). The functional coating and lattice information were characterized by high-resolution transmission electron microscopy (HRTEM, FEI G2 S-Twin). The element valence was analyzed by the X-ray photoelectron spectrometer (XPS, ESCALABMKLL). The crystal structure was examined by the powder X-ray diffractometer (XRD, Bruker D8 Advance) from 10° to 80° at a scan speed of 1 °·min^{-1}. The above XRD equipped with a temperature control device was used for variable temperature *in-situ* XRD testing. The sample table material was Al_2O_3. The delithiated electrode material charged to 4.5 V was used for thermal stability testing. The sample was heated from 30 to 600 °C at a heating rate of 1 °C·min^{-1} under a vacuum, and a single XRD spectrum took 6 min from 15° to 75° (10 °·min^{-1}). The delithiated electrode material charged to 4.5 V was used for the differential scanning calorimeter (DSC, METTLER TOLEDO DSC3) test, which was performed from 125 to 300 °C at a heating rate of 2 °C·min^{-1} under an N_2 atmosphere. The above XRD with a NEWARE battery tester was used for battery *in-situ* XRD testing. The battery was cycled once under 20 mA·g^{-1} current density. A single XRD spectrum took 12 min from 10° to 80°.

2.3 Electrochemical measurement

The cathode electrode was prepared as follows: active material, C45, KS-6, and PVDF (90:4.5:3:2.5, by weight) in NMP solution were evenly stirred and cast on an Al foil with an active-material loading of about 5.0 mg·cm^{-2}. Then they were vacuum dried and cut into circular electrodes (diameter 12 mm). CR2025 coin cell was used to characterize the electrochemical performances of materials. Li foil was used as the counter electrode for half-cell. The electrolyte was 1.0 M $LiPF_6$ in ethyl carbonate and ethyl methyl carbonate (EC:EMC = 3:7 by volume). The commercial graphite was used as the anode material for full cell. The electrode was prepared as follows: active material, C45, CMC, and SBR (90:6:2:2, by weight) in deionized water were evenly stirred and cast on a Cu foil. Then they were vacuum dried and cut into circular electrodes (diameter 12 mm). The N/P ratio was controlled at about 1.2. And the electrolyte was the above electrolyte plus 2 wt.% vinylene carbonate (VC) additive. The matched positive and negative electrode sheets were assembled in a CR2025 type coin cell to characterize the electrochemical

performance of the full cell. Galvanostatic charge/discharge was tested by the NEWARE battery tester. BioLogic VMP3 electrochemical workstation was used to test electrochemical impedance spectroscopy (EIS) and cyclic voltammetry (CV) data. The EIS test was performed by applying an amplitude of 5 mV in the frequency range of 100 mHz to 200 kHz when fully discharged to 3.0 V at different cycles. For GITT, the result was obtained by charging and discharging the cells for 30 minutes at the 20 $mA{\cdot}g^{-1}$ rate between 3.0 and 4.5 V followed by 120 min of relaxation time for each interval.

3 Results and discussion

3.1 Synthesis, morphology, and structure analysis

The schematic shown in Fig. 1(a) illustrates the NASICON-type $Li_3V_2(PO_4)_3$ coating modification engineering through a simple liquid phase stirring mixing and solid phase dry annealing method. Briefly, the pristine NCM sample is added to an acidic aqueous solution of $NH_4H_2PO_4$, and the alkaline residual lithium species on the particle surface would be dissolved after stirring. Then, a mixed solution of H_4NO_3V and $C_2H_2O_4$ is added, wherein the $C_2H_2O_4$ complexing agent could reduce the precipitation speed of H_4NO_3V, which is beneficial to the uniform coating of $Li_3V_2(PO_4)_3$. During the stirring process, the NCM sample coated with $Li_3V_2(PO_4)_3$-based films is obtained by drying in a water bath. Finally, the obtained powder is annealed in the air to obtain $Li_3V_2(PO_4)_3$-coated NCM samples. Figures 1(b) and 1(c) and Fig. S2 in the ESM show the SEM images of the pristine NCM and NCM@LVP samples, note that the particle surface of NCM@LVP has a passivation film and no island particle formation. The interplanar spacing of 0.209 nm is the typical (104) plane of the pristine NCM samples (Fig. 1(d)). The HRTEM image of the NCM@LVP sample shows a 7 nm thick dense, smooth, and uniform coating layer, and the interplanar spacing corresponds well to the (121) plane of $Li_3V_2(PO_4)_3$ (Fig 1(e)). And Ni, Co, Mn, P, and V elements are all uniformly distributed throughout the particle (Figs. 1(f)– 1(k)). Figure 1(l) and Fig. S3 in the ESM displays the XRD patterns and refinement results of the pristine NCM and NCM@LVP samples. Their main diffraction peaks can be indexed to a hexagonal layered structure with the *R*3*m* space group [45]. And no obvious $Li_3V_2(PO_4)_3$ diffraction peaks are detected, which may be caused by too little amount of $Li_3V_2(PO_4)_3$. XPS is also used to further characterize the element valence of the material. The two characteristic peaks of Ni 2p correspond well to Ni^{2+} and Ni^{3+} (Fig. 1(m)), and no obvious peak shift is found for the pristine NCM and NCM@LVP samples, which implies that the $Li_3V_2(PO_4)_3$ coating layer did not change the pristine structure of the active material [16]. The characteristic peaks of V 2p (Fig. 1(n)) and P 2p (Fig. 1(o)) located at 517.4 and 132.9 eV corresponds well to V^{3+} and P^{3+}, respectively [22, 34]. These results demonstrate that the introduced *in-situ* coating engineering utilizing residual lithium has a good coating effect, which will be beneficial to improving the lithium storage performance of high-voltage medium-nickel low-cobalt cathode materials.

3.2 Electrochemical performance

The electrochemical performances of the pristine NCM and NCM@LVP samples are fully examined and compared to investigate the superiority of the NASICON-type $Li_3V_2(PO_4)_3$ functional coating under the high cut-off voltage of 4.5 V. Figures 2(a) and 2(b) show their cyclic voltammetry (CV) curves of first five cycles. They all contain two pairs of common redox peaks (i.e., low voltage: $Ni^{2+/3+}$ and Ni^{4+}; high voltage: Co^{3+} and Co^{4+}), and the broad oxidation peak at about 4.0 V in the first cycle is related to the formation of the cathode electrolyte interface (CEI) film [8]. It can be seen that the CV curves of NCM@LVP have better reversibility than the pristine NCM after the first charge and discharge, which implies that $Li_3V_2(PO_4)_3$ coating can enhance the

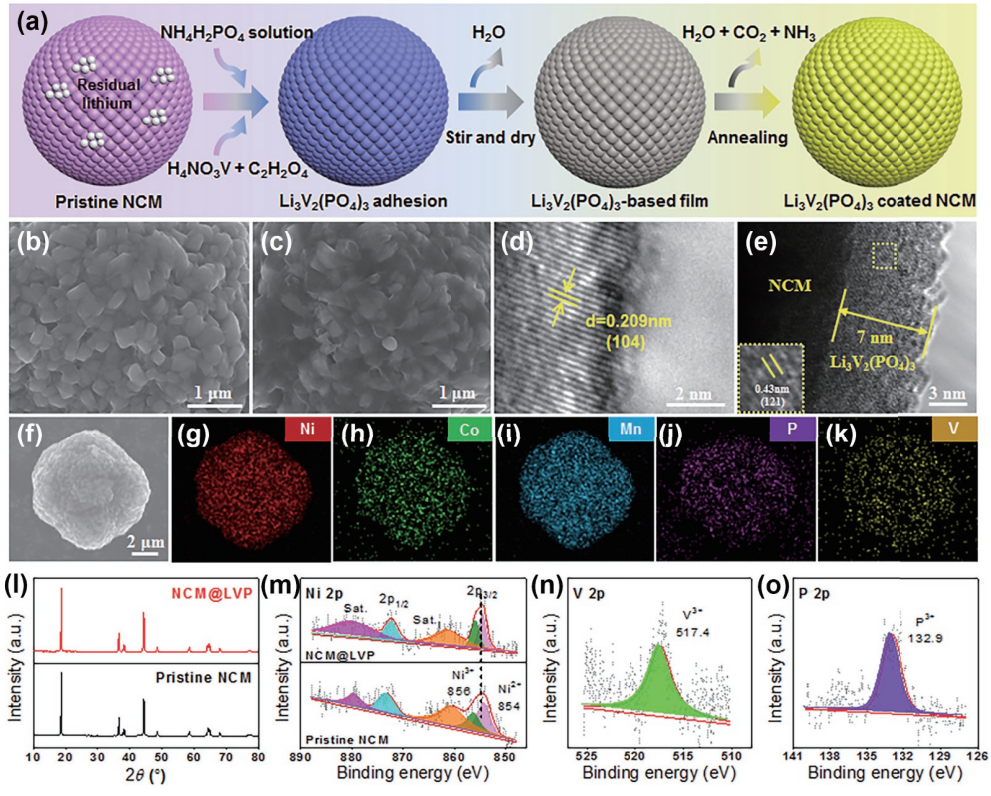

Figure 1 (a) Schematic of the synthesis procedure of NASICON-type $Li_3V_2(PO_4)_3$ coated NCM. (b) and (c) The particle surface SEM images and (d) and (e) HRTEM images of the pristine NCM and NCM@LVP samples. (f)–(k) EDS elemental mapping of the NCM@LVP sample. (l) XRD patterns and (m) XPS data of Ni element of the pristine NCM and NCM@LVP samples. (n) and (o) XPS data of V and P elements of the NCM@LVP sample.

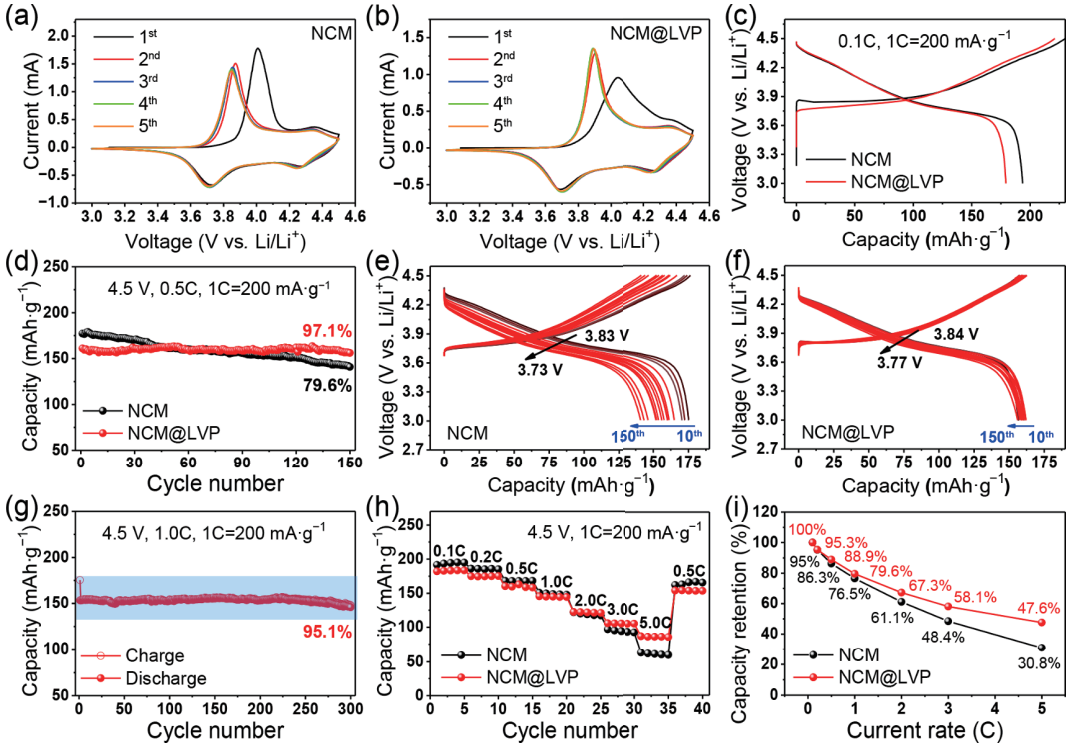

Figure 2 Comparison of (a) and (b) CV curves, (c) initial charge/discharge curves, (d) cycle performance, and (e) and (f) the corresponding charge/discharge curves from the 10th cycle to 150th cycle of the pristine NCM and NCM@LVP samples under 4.5 V high voltage. (g) The long cycle performance for the NCM@LVP sample at 1.0 C current density and 4.5 V high voltage. Comparison of (h) rate performance and (i) capacity retention rate of different current rates relative to the initial capacity of the pristine NCM and NCM@LVP samples.

electrode-electrolyte interface stability and bulk structure stability of the material. The initial discharge specific capacity of NCM@LVP is slightly smaller (180 mAh·g^{-1} *vs.* 188 mAh·g^{-1}) than the pristine NCM (Fig. 2(c)), which is caused by the mass fraction of the $Li_3V_2(PO_4)_3$ coating and a slightly lower initial Coulombic efficiency. Figure 2(d) exhibits their cycle performance at 0.5 C current density. Although the specific capacity of NCM@LVP is lower than that of NCM at the beginning, NCM@LVP maintains a higher specific capacity (156 mAh·g^{-1} vs. 141 mAh·g^{-1}) and capacity retention rate (97.1% vs. 79.6%) than NCM after 150 cycles. And their corresponding charge-discharge curves from the 10th to the 150th cycle are also depicted in Figs. 2(e) and 2(f). NCM@LVP has a smaller discharge median voltage attenuation than the pristine NCM. NCM@LVP declines from 3.84 to 3.77 V (0.07 V), and NCM declines from 3.83 to 3.73 V (0.1 V). Figure 2(g) investigates the long cycle performance of the NCM@LVP sample at a 1.0 C high current density. A high specific capacity of 146 mAh·g^{-1} is still maintained after 300 cycles, with a capacity retention rate of 95.1%. And their Coulombic efficiency is almost kept above 99% in the whole cycle (Fig. S4 in the ESM). And the NCM@LVP sample also shows superior cycle stability compared to the results reported in the literature of other coating modification studies (Table S1 in the ESM) [46–48]. In addition to the cycle stability performance, their rate performances are also evaluated in Fig. 2(h). Note that the sample with the $Li_3V_2(PO_4)_3$ coating has a better rate performance, NCM@LVP can output a specific capacity of 87 mAh·g^{-1} at a high current density of 5 C, while the pristine NCM is only 58 mAh·g^{-1}, and NCM@LVP has a higher capacity retention rate (47.6% vs. 30.8%) relative to the initial capacity compared to the pristine NCM (Fig. 2(i)). The improved cycling stability and rate performance can be attributed to the enhanced electrode-electrolyte interfacial stability and bulk layered structure stability, due to the stable three-dimensional network framework and high ionic and electronic conductivity of NASICON-type $Li_3V_2(PO_4)_3$ functional coating [49]. And to investigate the origin of the significantly improved electrochemical performance of NCM@LVP, we also systematically evaluate various aspects as described below.

3.3 Lithium diffusion kinetic and interfacial stability analysis

The galvanostatic intermittent titration technique (GITT) is used to evaluate the effect of $Li_3V_2(PO_4)_3$ coating on lithium diffusion kinetics. Figures 3(a) and 3(b) show the GITT curves of the third discharge process and the calculated actual lithium diffusion coefficients (D_{Li^+}) at different voltages for the pristine NCM and NCM@LVP samples. D_{Li^+} of the material can be calculated by the simplified equation [8].

$$D_{Li^+} = (4/\pi\tau) \times (m_B V_M / M_B S)^2 \times (E_S/E_\tau)^2 (\tau \ll L^2/D)$$
$$m_B V_M / M_B S = R_p/3$$

The R_p is the radius of the agglomerate particle (i.e., 5 μm). The τ, ΔE_S, and ΔE_τ values can be obtained as shown by a single GITT curve in Fig. S5 in the ESM. It can be seen that the D_{Li^+} of the NCM@LVP is about $10^{-8.7}$ cm^2·s^{-1}, which is higher than the average D_{Li^+} value of $10^{-8.9}$ cm^2·s^{-1} of the pristine NCM. The result declares that $Li_3V_2(PO_4)_3$ coating enhances the diffusion ability of lithium. The cyclic voltammetry measurements at different scan rates are also performed to qualitatively compare the lithium diffusion capabilities of the pristine NCM and NCM@LVP samples (Fig. 3(c) and Fig. S6 in the ESM). The apparent lithium diffusion coefficient is analyzed through the Randles–Sevcik equation [25].

$$Ip = 2.68 \times 10^5 n^{3/2} A D^{1/2} C \omega^{1/2} \qquad K = 2.68 \times 10^5 n^{3/2} A D^{1/2} C$$

The n (number of electron transfers), A (electrode area), and C (lithium molar concentration) are the relatively consistent fixed value for NCM and NCM@LVP samples. The plot of oxidation/reduction peak current (Ip) and the square root of the scan rate ($\omega^{1/2}\omega^{1/2}$) is shown in Fig. 3(d), which all show a linear

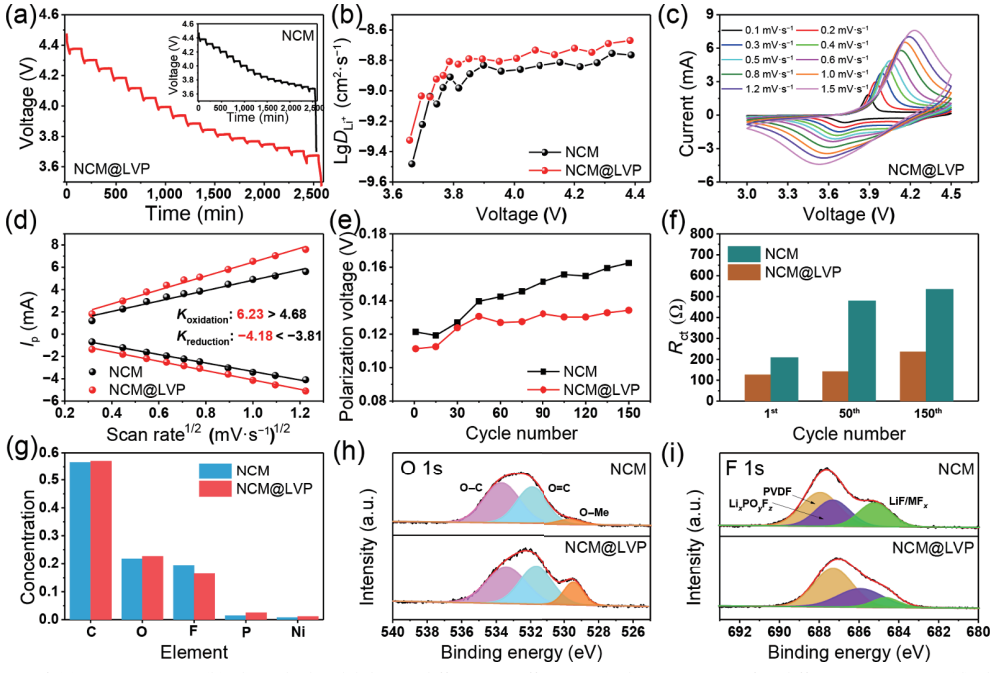

Figure 3 Comparison of (a) GITT curves, (b) the calculated lithium diffusion coefficient, (c) the CV curves for different scan rates, (d) the linear fit between oxidation/reduction peak current (*Ip*) and the square root of the scan rate (ω_∞), (e) the overall polarization voltage, (f) the interface charge transfer impedance of /different cycles, (g) the elemental concentration, (h) O 1s, and (i) F 1s XPS patterns after 150 cycles for the pristine NCM and NCM@LVP samples.

relationship. It can be inferred that the slope is proportional to the apparent lithium diffusion coefficient, the larger the slope, the faster the lithium diffusion rate. Then we can see that NCM@LVP exhibits a larger slope than the pristine NCM, which further indicates that NASICON-type $Li_3V_2(PO_4)_3$ high ionic and electronic conductivity functional coating enhances the lithium diffusion kinetics during charge and discharge.

NCM@LVP also shows a smaller overall polarization voltage compared to the pristine NCM (Fig. 3(e)), which can be attributed to the $Li_3V_2(PO_4)_3$ functional coating that improves the electrode-electrolyte interface environment (e.g., reduced interface side reactions and harmful surface phase transitions) [46]. The electrochemical impedance spectra (EIS) of the 1st, 50th, and 150th cycles for the pristine NCM and NCM@LVP samples after two activations are also tested (Fig. S7 in the ESM), and the fitting results show that the NCM@LVP has a smaller interface charge transfer impedance (R_{ct}) than the pristine NCM (Fig. 3(f)), which is due to the increased conductivity and weaker interface side reactions [44]. XPS is also used to check the surface chemistry differences of the pristine NCM and NCM@LVP samples after 150 cycles. Their elemental concentration comparison is shown in Fig. 3(g). The O element concentration increases after $Li_3V_2(PO_4)_3$ coating, which may be due to more Me-O bonds. Besides, the Ni content for the NCM@LVP is higher than the pristine NCM. The higher Me-O bond content and Ni content imply the formation of thin CEI films due to fewer electrode-electrolyte interfacial side reactions [50]. Noted that the O-Me peak of the NCM@LVP sample seems to be stronger (Fig. 3(h)), which implies less interfacial lattice oxygen loss after $Li_3V_2(PO_4)_3$ coating [16]. The LiF/MF_x peak for the NCM@LVP sample is also weaker (Fig. 3(i)), which indicates less electrolyte decomposition and transition metal dissolution [8]. These results suggest that the NASICON-type $Li_3V_2(PO_4)_3$ coating modification greatly maintains the stability of the electrode electrolyte interface.

3.4 Thermal stability and bulk structural stability analysis

Poor thermal stability is the main cause of battery thermal runaway and combustion, which greatly threatens the safety of the battery. And the thermal stability of the material is related to the stability of the electrode-electrolyte interface and bulk structure. Under high-temperature conditions, the oxygen release and the structural damage of the material are intensified, which will promote the occurrence of the undesired interface side reactions, harmful phase transitions, and lattice oxygen release [51]. The high-temperature self-discharge test is performed to examine the effect of the $Li_3V_2(PO_4)_3$ coating modification on thermal stability. At a high temperature of 60 °C, the half-cell is first charged to 4.5 V, then rested for 24 h, and finally discharged to 3.0 V. During the charging process, the pristine NCM delivers a higher charge capacity (259 mAh·g^{-1} vs. 237 mAh·g^{-1}) compared to the NCM@LVP due to the more intense interface reaction between the cathode and the electrolyte (Fig. 4(a)). The open-circuit voltage (OCV) during high-temperature storage of the pristine NCM suffers a severe decay and eventually left at only 4.14 V (Fig. 4(b)), and it can only maintain a discharge capacity of 132 mAh·g^{-1} after storage (Fig. 4(c)). However, NCM@LVP shows better thermal stability, its OCV remains as high as 4.26 V, and it can still output a high discharge capacity of 158 mAh·g^{-1} after storage. The high-temperature self-discharge test shows that $Li_3V_2(PO_4)_3$ functional coating can effectively reduce the reactivity of the cathode material and electrolyte under high voltage and high temperature. The cycle performance of the pristine NCM and NCM@LVP samples at a high operating temperature of 50 °C are also tested (Fig. 4(d)), noting that the NCM@LVP has a higher capacity retention rate and Coulombic efficiency, which further illustrates the beneficial improvement effect of $Li_3V_2(PO_4)_3$ functional coating. The differential scanning calorimeter (DSC) analyses of the pristine NCM and NCM@LVP samples in the deep delithiation state are also performed to directly evaluate the structural stability of the material under high temperature (Fig. 4(e)). When the material is heated at a high temperature, the delithiated material will undergo structural degradation and phase transition, along with the breaking of the Me-O bond and the release of lattice oxygen, which will generate a lot of heat. It can be seen that the heat release onset temperature of NCM@LVP is higher than that of the pristine NCM (229.2 °C vs. 213.1 °C), which shows enhanced structural stability under high temperature after $Li_3V_2(PO_4)_3$

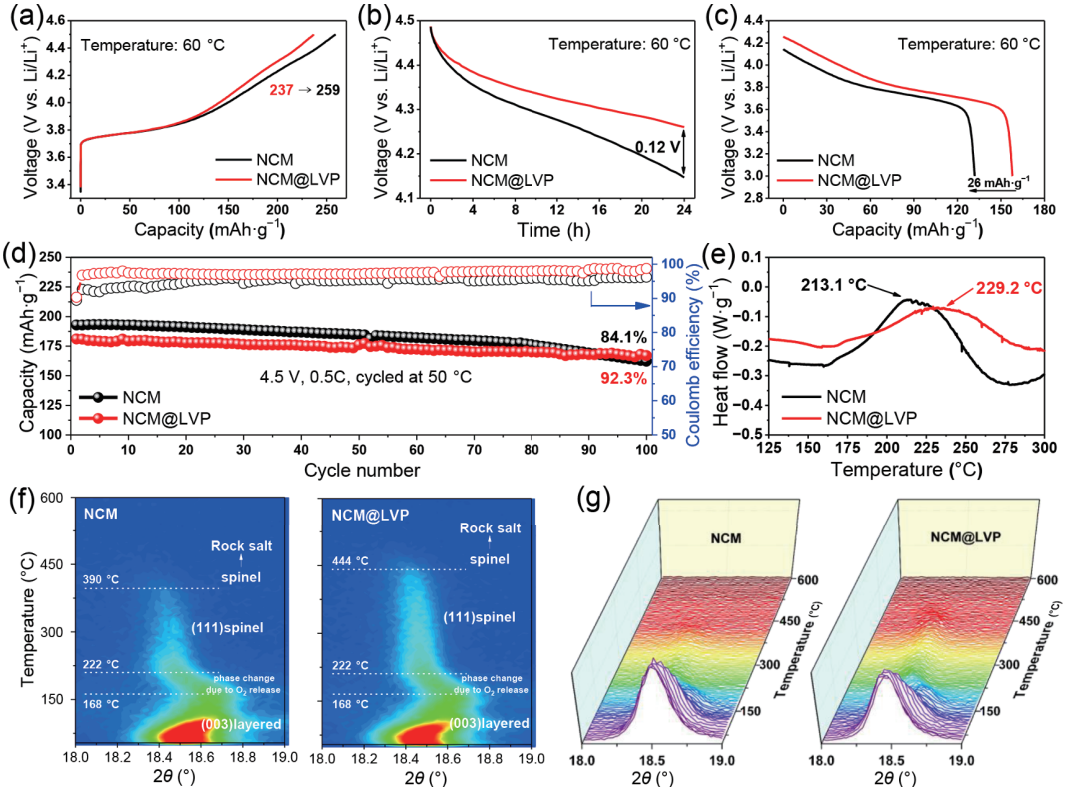

Figure 4 Self-discharge behavior of the pristine NCM and NCM@LVP samples at 60 °C: (a) charge curves, (b) open-circuit voltage (OCV) behavior during rest for 24 h, and (c) the following discharge curves after resting. (d) The high-temperature cycle performance, (e) DSC analysis results, (f) and (g) the contour plots and the corresponding peak shifts of the (003) reflection of the variable temperature in-situ XRD for the pristine NCM and NCM@LVP samples.

coating. Further, the variable temperature *in-situ* XRD is also used to evaluate the structural stability of the pristine NCM and NCM@LVP samples under high temperatures (Figs. 4(f) and 4(g)). Noted that the (003) diffraction peak shifts and disappears with the increase of temperature, which is accompanied by the phase transition process (layered → spinel → rock salt phase), and the phase transition is initiated by the oxygen evolution from the lattice due to the thermal instability [52]. Noted the onset temperature for NCM@LVP is considerably delayed as compared to the pristine NCM, reflecting an enhanced lattice oxygen framework stability, which corresponds well to the stable structural skeleton of the $Li_3V_2(PO_4)_3$ functional coating. These results indicate that the NASICON-type $Li_3V_2(PO_4)_3$ functional coating can greatly improve the thermal stability of the material by increasing the stability of the lattice oxygen framework and reducing the reaction activity of the cathode material.

The effect of the $Li_3V_2(PO_4)_3$ functional coating on the bulk structure stability of the high-voltage cathode material is also evaluated. The battery *in-situ* XRD is performed to observe the detailed structural evolution of the pristine NCM and NCM@LVP samples. Figures 5(a) and 5(b) show the contour plot of the (003) and (101) peaks and the corresponding voltage-capacity curves. They all show a similar structural evolution process to the previous research [53, 54]: the (003) peak initially shifts toward a lower 2θ angle, implying an increase in the *c*-axis, which is due to the increasing electrostatic repulsion between the oxygen anions at adjacent layers after part of the lithium is extracted. The process corresponds to the transition from the H1 to H2 phase. Then the (003) peak sharply shifts toward a higher 2θ angle, suggesting the steep shrinkage of the *c*-axis, which is because the gravity effect is greater than the electrostatic repulsion after a large amount of lithium is extracted. The process corresponds to the transition from the H2 to H3 phase. Noted that the *c*-axis shrinkage process (H2 to H3) is more rapid and aggressive than the *c*-axis expansion (H1 to H2), which will lead to a serious accumulation of internal strain and destroy the layered structural stability of the material. Especially under high voltage conditions, more lithium ions are released and cause a more serious phase transition from H2 to H3. And the (101) peak continues to turn to a higher 2θ angle during the whole charging process, implying the shrinkage of the *a*-axis and *b*-axis, which is due to the oxidation of transition metal ions and having a smaller ion radius. However, it is easy to see that there are still some differences between the two samples. Firstly, regarding the H1 to H2 phase transition process, the pristine NCM exhibits a two-phase reaction mechanism: the formation of the H2 phase and the disappearance of the H1 phase exist at the same time. It is worth noting that the coexistence of two phases is essentially accompanied by strong internal strain from the significant lattice mismatch in the two-phase region [55]. Then it means that the pristine NCM sample will suffer a severe structural strain. But noted that NCM@LVP exhibits a nearly single-phase reaction mechanism. Secondly, relating the H2 to the H3 phase transition process, noted that the pristine NCM turns to a higher angle compared to the NCM@LVP, a more severe degree of H2 to H3 phase transition (0.388° vs. 0.306°), which implies that the pristine NCM has a greater degree of *c*-axis shrinkage (i.e., greater volume change) [35]. Then the weakened anisotropic internal stress for the NCM@LVP will inhibit the generation of intergranular microcracks, thereby maintaining the structural integrity of the secondary agglomerate particles [56, 57]. These beneficial improvements can be attributed to the $Li_3V_2(PO_4)_3$ with stable structures capable of constraining the expansion and contraction of the bulk structure. Figures 5(c) and 5(d) show the particle morphology of the pristine NCM and NCM@LVP samples after 150 cycles. It can be seen that there is a thick electrolyte interface film on the pristine NCM particle, while the structure and surface of the NCM@LVP particle are intact, which corresponds well to the above improved electrode-electrolyte interfacial stability and bulk structural stability [58–60]. Figure 5(e) displays the XRD patterns of the pristine NCM and

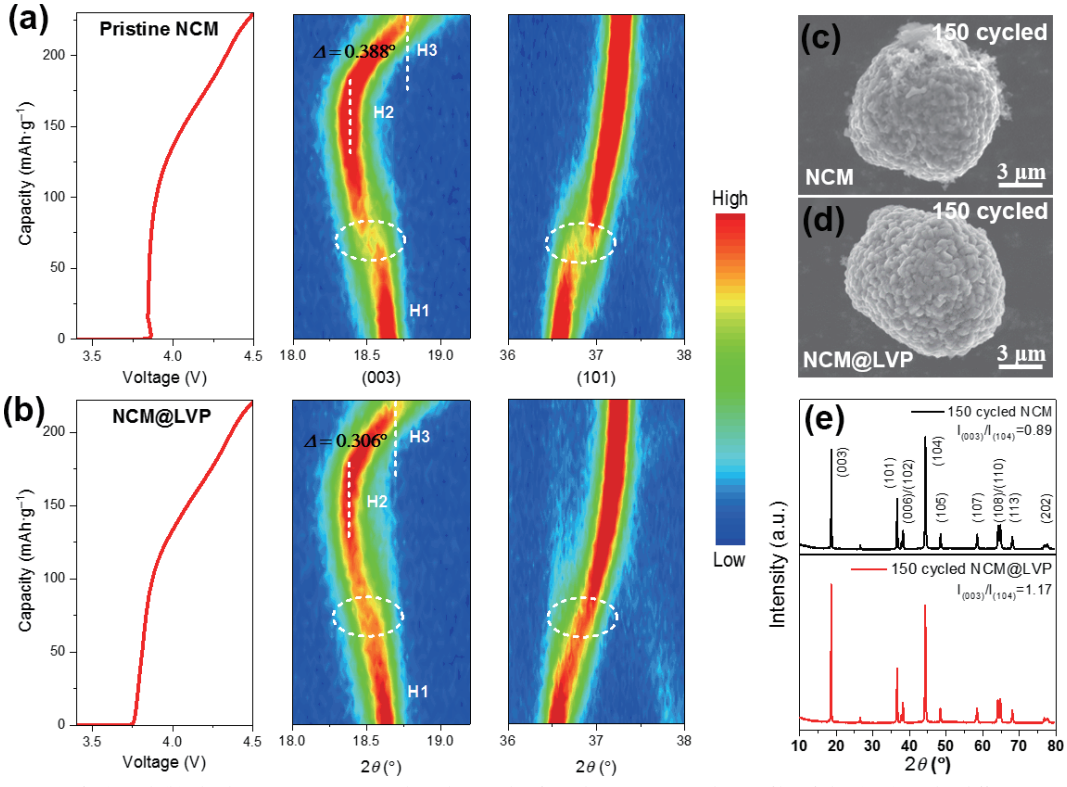

Figure 5 Comparison of (a) and (b) the battery in-situ XRD data during the first charge process: the profile of the (003) peaks diffraction patterns with the corresponding voltage-capacity curve, (c) and (d) SEM images after 150 cycles, and (e) the XRD patterns after 150 cycles for the pristine NCM and NCM@LVP samples.

NCM@LVP samples after 150 cycles. They all still maintain a well-layered structure. The difference is that the NCM@LVP has a larger $I_{(003)}/I_{(104)}$ ratio (1.17 vs. 0.89) compared to the pristine NCM, which implies a weakened Li^+/Ni^{2+} mixing and enhanced layer structure stability after $Li_3V_2(PO_4)_3$ coating [16]. These excellent improvement effects can be attributed to the restraint and passivation ability of the $Li_3V_2(PO_4)_3$ rigid functional coating on the structural changes of the material.

3.5 Electrochemical performances of full-battery

The superior lithium storage performance derived from the improved lithium diffusion kinetics, the electrode-electrolyte interface stability, thermal stability, and bulk structure stability after $Li_3V_2(PO_4)_3$ coating can also be further confirmed by using a high-voltage lithium-ion full battery with commercial graphite as the anode (Fig. 6(a) and Fig. S8 in the ESM). The capacity relationship between the negative and positive electrodes is controlled at 1.2 (i.e., N/P=1.2) by adjusting their active material loading, and the voltage range can be determined between 2.75–4.45 V (Fig. 6(b)). The initial charge and discharge curves are shown in Fig. 6(c). Figure 6(d) and Fig. S9 in the ESM exhibits the cycle performance at 0.5 C current density, and the designed full battery has a high capacity retention rate of 87.1% after 100 cycles. And it can also deliver a high specific capacity of 88 mAh·g^{-1} at a 5.0 C high current rate (Fig. 6(e) and Fig. S10 in the ESM). The energy density of the designed full battery is also calculated by the model formula [44] shown in Fig. 6(f), and it can reach a high energy density of 240 Wh·kg^{-1}. These results indicate that NASICON-type $Li_3V_2(PO_4)_3$ coated high-voltage medium-nickel low-cobalt cathode materials have great potential in the pursuit of high-energy-density LIB practical applications.

4 Conclusions

In summary, NCM60535 is successfully modified by utilizing residual lithium to form a typical NASICON-type $Li_3V_2(PO_4)_3$ functional coating in situ. The obtained NCM@LVP sample delivers a higher capacity retention rate (97.1% vs. 79.6%) after 150 cycles and a superior rate capacity (87 mAh·g^{-1} vs. 58 mAh·g^{-1}) at a 5.0 C current density than the pristine NCM under a high cut-off voltage of 4.5 V. This excellent cycle stability and rate performance is related to its improved lithium diffusion kinetics, electrode electrolyte interface stability, thermal stability, and bulk structure stability. These improvements are attributed to the removal of surface residual lithium and the formation of NASICON-type $Li_3V_2(PO_4)_3$ functional coatings with stable structure and high ionic and electronic conductivity. The ultrathin, uniform, and dense coating physically blocks the direct contact between the electrode and the electrolyte, thereby reducing the occurrence of side reactions at the interface. The stable framework structure and high ionic/electronic conductivity can constrain the volume change of the layered structure and enhance the ion/electron transport rate, thereby improving the layered structure stability and enhancing the rate performance. Not only this $Li_3V_2(PO_4)_3$, but other NASICON-type materials (e.g., $LiZr_2(PO_4)_3$, $LiTi_2(PO_4)_3$, $LiGe_2(PO_4)_3$, and so on) also have such excellent effects because of their similar properties. Then we suggest that NASICON-type materials obtained by utilizing residual lithium are a preferred coating material candidate for improving the lithium storage performance of high-voltage medium-nickel low-cobalt cathode materials.

Acknowledgements

This research is funded by the National Key R&D Program of China (No. 2017YFE0198100), the National Natural Science Foundation of China (No. 21975250), the Key R&D Program of Jilin Province (No. 20220201132GX), the Key R&D Program of Hubei Province (No. 2022BAA084), and the Capital Construction Fund Projects within the Budget of Jilin Province (2021C037-2).

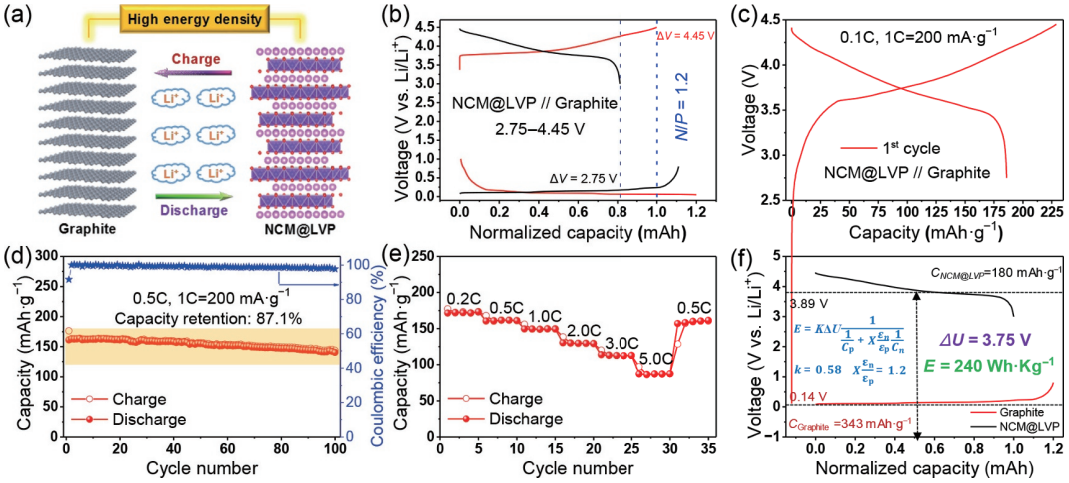

Figure 6 (a) Schematic configuration of the high-voltage high-energy-density lithium-ion full battery consisting of the NCM@LVP cathode and a commercial graphite anode. (b) Negative and positive (N/P) matching relationship. (c) The initial charge/discharge curves, (d) cycle performance, and (e) rate performance of the designed lithium-ion full battery. (f) Calculation of energy density for the full battery, where the k value in the empirical model was supposed as 0.58.

Electronic Supplementary Material: Supplementary material (comparison of cycling stability with related materials reported in recent literature. Electrochemical performance of NCM@LVP samples under different annealing temperatures. SEM images, XRD refinement, Coulombic efficiency, single GITT curves, CV curves for different scan rates, and the electrochemical impedance spectroscopy of different cycles of the pristine NCM and NCM@LVP samples. Graphite SEM images, charge and discharge curves corresponding to cycle and rate performance for full battery) is available in the online version of this article at https://doi.org/10.1007/s12274-022-5298-y.

References

[1] Li, W. D.; Erickson, E. M.; Manthiram, A. High-nickel layered oxide cathodes for lithium-based automotive batteries. *Nat. Energy* **2020**, *5*, 26–34.

[2] Liu, J. X.; Wang, J. Q.; Ni, Y. X.; Zhang, K.; Cheng, F. Y.; Chen, J. Recent breakthroughs and perspectives of high-energy layered oxide cathode materials for lithium ion batteries. *Mater. Today* **2021**, *43*, 132–165.

[3] Liu, W.; Oh, P.; Liu, X. E.; Lee, M. J.; Cho, W.; Chae, S.; Kim, Y.; Cho, J. Nickel-rich layered lithium transition-metal oxide for high-energy lithium-ion batteries. *Angew. Chem., Int. Ed.* **2015**, *54*, 4440–4457.

[4] Wu, K.; Li, Q.; Dang, R. B.; Deng, X.; Chen, M. M.; Lee, Y. L.; Xiao, X. L.; Hu, Z. B. A novel synthesis strategy to improve cycle stability of $LiNi_{0.8}Mn_{0.1}Co_{0.1}O_2$ at high cut-off voltages through core-shell structuring. *Nano Res.* **2019**, *12*, 2460–2467.

[5] Zhuang, Z. C.; Li, Y. H.; Yu, R. H.; Xia, L. X.; Yang, J. R.; Lang, Z. Q.; Zhu, J. X.; Huang, J. Z.; Wang, J. O.; Wang, Y. et al. Reversely trapping atoms from a perovskite surface for high-performance and durable fuel cell cathodes. *Nat. Catal.* **2022**, *5*, 300–310.

[6] Jiang, M.; Danilov, D. L.; Eichel, R. A.; Notten, P. H. L. A review of degradation mechanisms and recent achievements for Ni-rich cathode-based Li-ion batteries. *Adv. Energy Mater.* **2021**, *11*, 2103005.

[7] Zhao, H.; Lam, W. Y. A.; Sheng, L.; Wang, L.; Bai, P.; Yang, Y.; Ren, D. S.; Xu, H.; He, X. M. Cobalt-free cathode materials: Families and their prospects. *Adv. Energy Mater.* **2022**, *12*, 2103894.

[8] Shen, Y. B.; Yao, X. J.; Zhang, J. H.; Wang, S. H.; Zhang, D. Y.; Yin, D. M.; Wang, L. M.; Zhang, Y. H.; Hu, J. H.; Cheng, Y. et al. Sodium doping derived electromagnetic center of lithium layered oxide cathode materials with enhanced lithium storage. *Nano Energy* **2022**, *94*, 106900.

[9] Hao, J. C.; Zhuang, Z. C.; Cao, K. C.; Gao, G. H.; Wang, C.; Lai, F. L.; Lu, S. L.; Ma, P. M.; Dong, W. F.; Liu, T. X. et al. Unraveling the electronegativity-dominated intermediate adsorption on high-entropy alloy electrocatalysts. *Nat. Commun.* **2022**, *13*, 2662.

[10] Liu, T. C.; Yu, L.; Liu, J. J.; Lu, J.; Bi, X. X.; Dai, A.; Li, M.; Li, M. F.; Hu, Z. X.; Ma, L. et al. Understanding Co roles towards developing Co-free Ni-rich cathodes for rechargeable batteries. *Nat. Energy* **2021**, *6*, 277–286.

[11] Kim, Y.; Park, H.; Warner, J. H.; Manthiram, A. Unraveling the intricacies of residual lithium in high-Ni cathodes for lithium-ion batteries. *ACS Energy Lett.* **2021**, *6*, 941–948.

[12] Yang, W.; Xiang, W.; Chen, Y. X.; Wu, Z. G.; Hua, W. B.; Qiu, L.; He, F. R.; Zhang, J.; Zhong, B. H.; Guo, X. D. Interfacial regulation of Ni-rich cathode materials with an ion-conductive and pillaring layer by infusing gradient boron for improved cycle stability. *ACS Appl. Mater. Interfaces* **2020**, *12*, 10240–10251.

[13] Ryu, W. G.; Shin, H. S.; Park, M. S.; Kim, H.; Jung, K. N.; Lee, J. W. Mitigating storage-induced degradation of Ni-rich $LiNi_{0.8}Co_{0.1}Mn_{0.1}O_2$ cathode material by surface tuning with phosphate. *Ceram. Int.* **2019**, *45*, 13942–13950.

[14] Li, W. D.; Song, B. H.; Manthiram, A. High-voltage positive electrode materials for lithium-ion batteries. *Chem. Soc. Rev.* **2017**, *46*, 3006–3059.

[15] Liu, Z. H.; Du, Y.; Zhang, P. F.; Zhuang, Z. C.; Wang, D. S. Bringing catalytic order out of chaos with nitrogen-doped ordered mesoporous carbon. *Matter* **2021**, *4*, 3161–3194.

[16] Shen, Y. B.; Yao, X. J.; Wang, S. H.; Zhang, D. Y.; Yin, D. M.; Wang, L. M.; Cheng, Y. Gospel for improving the lithium storage performance of high-voltage high-nickel low-cobalt layered oxide cathode materials. *ACS Appl. Mater. Interfaces* **2021**, *13*, 58871–58884.

[17] Zhang, W.; Sun, Y. G.; Deng, H. Q.; Ma, J. M.; Zeng, Y.; Zhu, Z. Q.; Lv, Z. S.; Xia, H. R.; Ge, X.; Cao, S. K. et al. Dielectric polarization in inverse spinel-structured Mg_2TiO_4 coating to suppress oxygen evolution of Li-rich cathode materials. *Adv. Mater.* **2020**, *32*, 2000496.

[18] Wen, Y. K.; Zhuang, Z. C.; Zhu, H.; Hao, J. C.; Chu, K. B.; Lai, F. L.; Zong, W.; Wang, C.; Ma, P. M.; Dong, W. F. et al. Isolation of metalloid boron atoms in intermetallic carbide boosts the catalytic selectivity for electrocatalytic N_2 fixation. *Adv. Energy Mater.* **2021**, *11*, 2102138.

[19] Zhuang, Z. C.; Li, Y.; Li, Y. H.; Huang, J. Z.; Wei, B.; Sun, R.; Ren, Y. J.; Ding, J.; Zhu, J. X.; Lang, Z. Q. et al. Atomically dispersed nonmagnetic electron traps improve oxygen reduction activity of perovskite oxides. *Energy Environ. Sci.* **2021**, *14*, 1016–1028.

[20] Huang, X.; Zhu, W. C.; Yao, J. Y.; Bu, L. M.; Li, X. Y.; Tian, K.; Lu, H.; Quan, C. X.; Xu, S. G.; Xu, K. H. et al. Suppressing structural degradation of Ni-rich cathode materials towards improved cycling stability enabled by a Li_2MnO_3 coating. *J. Mater. Chem. A* **2020**, *8*, 17429–17441.

[21] Jiang, K. Z.; Guo, S. H.; Pang, W. K.; Zhang, X. P.; Fang, T. C.; Wang, S. F.; Wang, F. W.; Zhang, X. Y.; He, P.; Zhou, H. S.

Oxygen vacancy promising highly reversible phase transition in layered cathodes for sodium-ion batteries. *Nano Res.* **2021**, *14*, 4100–4106.

[22] Du, K.; Gao, A.; Gao, L. F.; Sun, S. W.; Lu, X.; Yu, C. Y.; Li, S. Y.; Zhao, H. L.; Bai, Y. Enhancing the structure stability of Ni-rich $LiNi_{0.6}Co_{0.2}Mn_{0.2}O_2$ cathode via encapsulating in negative thermal expansion nanocrystalline shell. *Nano Energy* **2021**, *83*, 105775.

[23] Lai, Y. J.; Li, Z. J.; Zhao, W. X.; Cheng, X. N.; Xu, S.; Yu, X.; Liu, Y. An ultrasound-triggered cation chelation and reassembly route to one-dimensional Ni-rich cathode material enabling fast charging and stable cycling of Li-ion batteries. *Nano Res.* **2020**, *13*, 3347–3357.

[24] Hao, J. C.; Zhuang, Z. C.; Hao, J. C.; Cao, K. C.; Hu, Y. X.; Wu, W. B.; Lu, S. L.; Wang, C.; Zhang, N.; Wang, D. S. et al. Strain relaxation in metal alloy catalysts steers the product selectivity of electrocatalytic CO_2 reduction. *ACS Nano* **2022**, *16*, 3251–3263.

[25] Cheng, Y.; Sun, Y.; Chu, C. T.; Chang, L. M.; Wang, Z. M.; Zhang, D. Y.; Liu, W. Q.; Zhuang, Z. C.; Wang, L. M. Stabilizing effects of atomic Ti doping on high-voltage high-nickel layered oxide cathode for lithium-ion rechargeable batteries. *Nano Res.* **2022**, *15*, 4091–4099.

[26] Yang, H. P.; Wu, H. H.; Ge, M. Y.; Li, L. J.; Yuan, Y. F.; Yao, Q.; Chen, J.; Xia, L. F.; Zheng, J. M.; Chen, Z. Y. et al. Simultaneously dual modification of Ni-rich layered oxide cathode for high-energy lithium-ion batteries. *Adv. Funct. Mater.* **2019**, *29*, 1808825.

[27] Yoon, M.; Dong, Y. H.; Hwang, J.; Sung, J.; Cha, H.; Ahn, K.; Huang, Y. M.; Kang, S. J.; Li, J.; Cho, J. Reactive boride infusion stabilizes Ni-rich cathodes for lithium-ion batteries. *Nat. Energy* **2021**, *6*, 362–371.

[28] Hao, J. C.; Zhuang, Z. C.; Hao, J. C.; Wang, C.; Lu, S. L.; Duan, F.; Xu, F. P.; Du, M. L.; Zhu, H. Interatomic electronegativity offset dictates selectivity when catalyzing the CO_2 reduction reaction. *Adv. Energy Mater.* **2022**, *12*, 2200579.

[29] Zhang, H. L.; Zhang, J. J. An overview of modification strategies to improve $LiNi_{0.8}Co_{0.1}Mn_{0.1}O_2$ (NCM811) cathode performance for automotive lithium-ion batteries. *eTransportation* **2021**, *7*, 100105.

[30] Kang, Q.; Li, Y.; Zhuang, Z. C.; Wang, D. S.; Zhi, C. Y.; Jiang, P. K.; Huang, X. Y. Dielectric polymer based electrolytes for high-performance all-solid-state lithium metal batteries. *J. Energy Chem.* **2022**, *69*, 194–204.

[31] Kim, J.; Ma, H.; Cha, H.; Lee, H.; Sung, J.; Seo, M.; Oh, P.; Park, M.; Cho, J. A highly stabilized nickel-rich cathode material by nanoscale epitaxy control for high-energy lithium-ion batteries. *Energy Environ. Sci.* **2018**, *11*, 1449–1459.

[32] Yao, L.; Liang, F. Q.; Jin, J.; Chowdari, B. V. R.; Yang, J. H.; Wen, Z. Y. Improved electrochemical property of Ni-rich $LiNi_{0.6}Co_{0.2}Mn_{0.2}O_2$ cathode via in-situ ZrO_2 coating for high energy density lithium ion batteries. *Chem. Eng. J.* **2020**, *389*, 124403.

[33] Xie, J.; Sendek, A. D.; Cubuk, E. D.; Zhang, X. K.; Lu, Z. Y.; Gong, Y. J.; Wu, T.; Shi, F. F.; Liu, W.; Reed, E. J. et al. Atomic layer deposition of stable $LiAlF_4$ lithium ion conductive interfacial layer for stable cathode cycling. *ACS Nano* **2017**, *11*, 7019–7027.

[34] Wu, Y. Q.; Ming, H.; Li, M. L.; Zhang, J. L.; Wahyudi, W.; Xie, L. Q.; He, X. M.; Wang, J.; Wu, Y. P.; Ming, J. New organic complex for lithium layered oxide modification: Ultrathin coating, high-voltage, and safety performances. *ACS Energy Lett.* **2019**, *4*, 656–665.

[35] Jamil, S.; Wang, G.; Yang, L.; Xie, X.; Cao, S.; Liu, H.; Chang, B. B.; Wang, X. Y. Suppressing H2-H3 phase transition in high Ni-low Co layered oxide cathode material by dual modification. *J. Mater. Chem. A* **2020**, *8*, 21306–21316.

[36] Zhai, Y. W.; Yang, W. Y.; Ning, D.; Yang, J. B.; Sun, L. M.; Schuck, G.; Schumacher, G.; Liu, X. F. Improving the cycling and air-storage stability of $LiNi_{0.8}Co_{0.1}Mn_{0.1}O_2$ through integrated surface/interface/doping engineering. *J. Mater. Chem. A* **2020**, *8*, 5234–5245.

[37] Kim, J. H.; Kim, H.; Choi, W.; Park, M. S. Bifunctional surface coating of $LiNbO_3$ on high-Ni layered cathode materials for lithium-ion batteries. *ACS Appl. Mater. Interfaces* **2020**, *12*, 35098–35104.

[38] Neudeck, S.; Walther, F.; Bergfeldt, T.; Suchomski, C.; Rohnke, M.; Hartmann, P.; Janek, J.; Brezesinski, T. Molecular surface modification of NCM622 cathode material using organophosphates for improved Li-ion battery full-cells. *ACS Appl. Mater. Interfaces* **2018**, *10*, 20487–20498.

[39] Fan, Q. L.; Yang, S. D.; Liu, J.; Liu, H. D.; Lin, K. J.; Liu, R.; Hong, C. Y.; Liu, L. Y.; Chen, Y.; An, K. et al. Mixed-conducting interlayer boosting the electrochemical performance of Ni-rich layered oxide cathode materials for lithium ion batteries. *J. Power Sources* **2019**, *421*, 91–99.

[40] Kim, J. M.; Zhang, X. H.; Zhang, J. G.; Manthiram, A.; Meng, Y. S.; Xu, W. A review on the stability and surface modification of layered transition-metal oxide cathodes. *Mater. Today* **2021**, *46*, 155–182.

[41] Chen, S. Q.; Wu, C.; Shen, L. F.; Zhu, C. B.; Huang, Y. Y.; Xi, K.; Maier, J.; Yu, Y. Challenges and perspectives for NASICON-type electrode materials for advanced sodium-ion batteries. *Adv. Mater.* **2017**, *29*, 1700431.

[42] Niu, Y. J.; Yu, Z. Z.; Zhou, Y. J.; Tang, J. W.; Li, M. X.; Zhuang, Z. C.; Yang, Y.; Huang, X.; Tian, B. B. Constructing stable Li-solid electrolyte interphase to achieve dendrites-free solid-state battery: A nano-interlayer/Li pre-reduction strategy. *Nano Res.* **2022**, *15*, 7180–7189.

[43] Hu, Q.; He, Y. F.; Ren, D. S.; Song, Y. Z.; Wu, Y. Z.; Liang, H. M.; Gao, J. H.; Xu, G.; Cai, J. Y.; Li, T. Y. et al. Targeted masking enables stable cycling of $LiNi_{0.6}Co_{0.2}Mn_{0.2}O_2$ at 4. 6 V. *Nano Energy* **2022**, *96*, 107123.

[44] Shen, Y. B.; Xue, H. J.; Wang, S. H.; Wang, Z. M.; Zhang, D. Y.; Yin, D. M.; Wang, L. M.; Cheng, Y. A highly promising high-nickel low-cobalt lithium layered oxide cathode material for high-performance lithium-ion batteries. *J. Colloid Interface Sci.* **2021**, *597*, 334–344.

[45] Liu, Y.; Tang, L. B.; Wei, H. X.; Zhang, X. H.; He, Z. J.; Li, Y. J.; Zheng, J. C. Enhancement on structural stability of Ni-rich cathode materials by *in-situ* fabricating dual-modified layer for lithium-ion batteries. *Nano Energy* **2019**, *65*, 104043.

[46] Liu, W.; Li, X. F.; Hao, Y. C.; Xiong, D. B.; Shan, H.; Wang, J. J.; Xiao, W.; Yang, H. J.; Yang, H.; Kou, L. et al. Functional passivation interface of $LiNi_{0.8}Co_{0.1}Mn_{0.1}O_2$ toward superior lithium storage. *Adv. Funct. Mater.* **2021**, *31*, 2008301.

[47] Xu, Q.; Li, X. F.; Kheimeh Sari, H. M.; Li, W. B.; Liu, W.; Hao, Y. C.; Qin, J.; Cao, B.; Xiao, W.; Xu, Y. et al. Surface engineering of $LiNi_{0.8}Mn_{0.1}Co_{0.1}O_2$ towards boosting lithium storage:Bimetallic oxides versus monometallic oxides. *Nano Energy* **2020**, *77*, 105034.

[48] Liu, S. Y.; Zhang, C. C.; Su, Q. L.; Li, L. Y.; Su, J. M.; Huang, T.; Chen, Y. B.; Yu, A. S. Enhancing electrochemical performance of $LiNi_{0.6}Co_{0.2}Mn_{0.2}O_2$ by lithium-ion conductor surface modification. *Electrochim. Acta* **2017**, *224*, 171–177.

[49] Li, L. J.; Xu, M.; Yao, Q.; Chen, Z. Y.; Song, L. B.; Zhang, Z. A.; Gao, C. H.; Wang, P.; Yu, Z. Y.; Lai, Y. Q. Alleviating surface degradation of nickel-rich layered oxide cathode material by encapsulating with nanoscale Li-ions/electrons superionic conductors hybrid membrane for advanced Li-ion batteries. *ACS Appl. Mater. Interfaces* **2016**, *8*, 30879–30889.

[50] Li, J. Y.; Li, W. D.; Wang, S. Y.; Jarvis, K.; Yang, J. H.; Manthiram, A. Facilitating the operation of lithium-ion cells with high-nickel layered oxide cathodes with a small dose of aluminum. *Chem. Mater.* **2018**, *30*, 3101–3109.

[51] Jeong, M.; Kim, H.; Lee, W.; Ahn, S. J.; Lee, E.; Yoon, W. S. Stabilizing effects of Al-doping on Ni-rich $LiNi_{0.80}Co_{0.15}Mn_{0.05}O_2$ cathode for Li rechargeable batteries. *J. Power Sources* **2020**, *474*, 228592.

[52] Wang, Y. Y.; Wang, Y. Y.; Liu, S.; Li, G. R.; Zhou, Z.; Xu, N.; Wu, M. T.; Gao, X. P. Building the stable oxygen framework in high-Ni layered oxide cathode for high-energy-density Li-ion batteries. *Energy Environ. Mater.* **2022**, *5*, 1260–1269.

[53] Mo, Y.; Guo, L. J.; Cao, B. K.; Wang, Y. G.; Zhang, L.; Jia, X. B.; Chen, Y. Correlating structural changes of the improved cyclability upon Nd-substitution in $LiNi_{0.5}Co_{0.2}Mn_{0.3}O_2$ cathode materials. *Energy Storage Mater.* **2019**, *18*, 260–268.

[54] Xie, Q.; Li, W. D.; Manthiram, A. A Mg-doped high-nickel layered oxide cathode enabling safer, high-energy-density Li-ion batteries. *Chem. Mater.* **2019**, *31*, 938–946.

[55] Li, J. Y.; Manthiram, A. A comprehensive analysis of the interphasial and structural evolution over long-term cycling of

ultrahigh-nickel cathodes in lithium-ion batteries. *Adv. Energy Mater.* **2019**, *9*, 1902731.

[56] Zhuang, Z. C.; Li, Y.; Huang, J. Z.; Li, Z. L.; Zhao, K. N.; Zhao, Y. L.; Xu, L.; Zhou, L.; Moskaleva, L. V.; Mai, L. *Sisyphus* effects in hydrogen electrochemistry on metal silicides enabled by silicene subunit edge. *Sci. Bull.* **2019**, *64*, 617–624.

[57] Zhuang, Z. C.; Huang, J. Z.; Li, Y.; Zhou, L.; Mai, L. Q. The holy grail in platinum-free electrocatalytic hydrogen evolution: Molybdenum-based catalysts and recent advances. *ChemElectroChem* **2019**, *6*, 3570–3589.

[58] Wang, C. L.; Gao, Y. X.; Sun, L. S.; Zhao, Y.; Yin, D. M.; Wang, H. R.; Cao, J. C.; Cheng, Y.; Wang, L. M. Anti-catalytic and zincophilic layers integrated zinc anode towards efficient aqueous batteries for ultra-long cycling stability. *Nano Res.* **2022**, *15*, 8076–8082.

[59] Jiang, J. Z.; Bai, S. S.; Zou, J.; Liu, S.; Hsu, J. P.; Li, N.; Zhu, G. Y.; Zhuang, Z. C.; Kang, Q.; Zhang, Y. Z. Improving stability of MXenes. *Nano Res.* **2022**, *15*, 6551–6567.

[60] Luo, L. X.; Fu, C. H.; Wu, A. M.; Zhuang, Z. C.; Zhu, F. J.; Jiang, F. L.; Shen, S. Y.; Cai, X. Y.; Kang, Q.; Zheng, Z. F. et al. Hydrogen-assisted scalable preparation of ultrathin Pt shells onto surfactant-free and uniform Pd nanoparticles for highly efficient oxygen reduction reaction in practical fuel cells. *Nano Res.* **2022**, *15*, 1892–1900.